Materials & Design 258 (2025) 114550

Contents lists available at ScienceDirect

Materials & Design

journal homepage: www.elsevier.com/locate/matdes

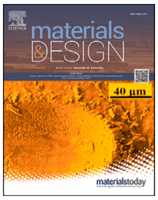

Designing microcompression experiments for nanoporous metals via computational plasticity

Tim Fischer [a,*], Norbert Huber [a,b]

[a] Institute of Materials Physics and Technology, Hamburg University of Technology, Eißendorfer Straße 42, Hamburg, D-21073, Germany
[b] Bundesanstalt für Materialforschung und -prüfung (BAM), Unter den Eichen 87, Berlin, D-12205, Germany

ARTICLE INFO

Keywords:
Nanoporous gold
Microcompression
Plasticity
Finite element method
Micromechanics

ABSTRACT

Micropillar compression testing is essential for understanding bulk metal plasticity at small scales and has emerged as a key technique for evaluating nanoporous metals like nanoporous gold (NPG). To support experimental design, we present a computational plasticity study on single crystal NPG micropillars, systematically examining four extrinsic factors: pillar height-to-diameter ratio ($1.5 \leq h/d \leq 2.5$), taper angle ($0 \leq \theta \leq 4^\circ$), friction coefficient ($0.0 \leq \mu \leq 0.2$), and misalignment angle ($0 \leq \alpha \leq 2^\circ$). The study reveals that NPG exhibits similar trends to its bulk counterpart but is less prone to post-yield buckling in unstable crystal orientations. For optimal NPG pillar stability, an aspect ratio of $1.5 \leq h/d \leq 2$ is recommended and a moderate taper angle ($\theta \approx 2^\circ$) to prevent artificial stiffening and yielding. Even minimal friction ($\mu \approx 0.05$) enhances stability, while buckling is mainly governed by misalignment, requiring $\alpha \leq 1^\circ$ to also avoid underestimating the elastic modulus.

1. Introduction

Nanoporous metals, including nanoporous gold (NPG), are a unique class of materials characterized by a bicontinuous network of nanoscale ligaments and pores, typically formed through dealloying processes. Their high surface area, low density, and tunable structural properties make them attractive for applications in catalysis, sensing, and energy storage [1–6]. Beyond functional properties, the mechanical behavior of nanoporous metals is of significant interest, particularly for their potential use in micro- and nanoscale devices [1,7]. Nanoporous metals exhibit distinct mechanical properties from their bulk counterparts due to their nanoscale architecture. Their strength is size-dependent, with ligament-scale plasticity playing a dominant role [8–16]. Despite low relative density, they achieve high strength-to-weight ratios and notable strain hardening. Deformation and failure mechanisms are governed by ligament orientation, strain localization, and surface effects, while crystallographic anisotropy seems to have a limited impact on yielding [17–24]. A detailed discussion of the microscopic failure behavior of NPG is provided in [25].

Advanced micromechanical testing methods, such as nanoindentation and micropillar compression, have been widely employed to investigate the mechanical behavior of bulk metals at small scales. While for instance microcompression experiments on single crystal bulk gold are reported in [26,27], gold nanowire microcompression/-bending are found in [28,29]. These techniques provide valuable insights into fundamental deformation mechanisms by isolating size effects and intrinsic material responses. More recently, these methods have been extended to nanoporous metals, offering a deeper understanding of their mechanical stability and deformation behavior [30–40]. Among these, micropillar compression has emerged as a powerful tool for probing the mechanical properties, enabling direct observation of plasticity and failure mechanisms. Moreover, this type of testing is increasingly relevant for a similar emerging class of architected cellular materials, where microstructural control enables tailored mechanical properties [41]. However, due to the intricate architecture of nanoporous metals, additional complexities such as extrinsic size effects, frictional influences, and misalignment during testing must be carefully considered. It is worth noting that, in addition to microcompression, microtensile testing of NPG has also been explored [30,42], however, this aspect is beyond the scope of the present study.

To facilitate result interpretation, provide mechanistic insights, and support experimental design, these complex tests are often supplemented by finite element method (FEM) simulations [43–55]. However, computational plasticity studies mainly focus on fully dense materials. Apart from macroscale FEM studies using representative volume elements (RVEs) [56–64], FEM simulations explicitly modeling nanoporous

---

* Corresponding author.
E-mail address: tim.fischer@tuhh.de (T. Fischer).

https://doi.org/10.1016/j.matdes.2025.114550
Received 15 May 2025; Received in revised form 1 July 2025; Accepted 8 August 2025

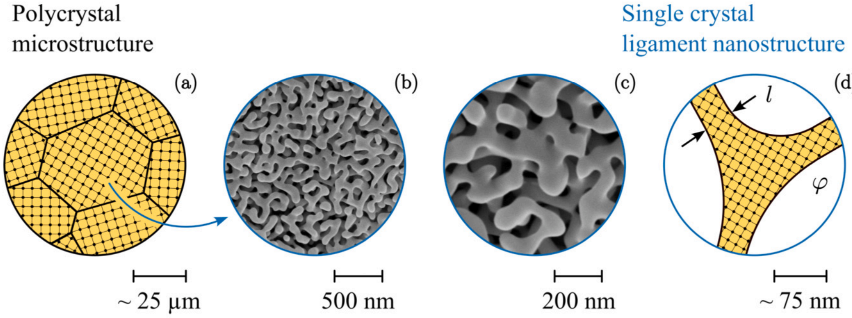

Fig. 1. Schematic representation of NPG across micro- and nanoscales. On the microscale (a), NPG is polycrystalline, while on the nanoscale (b-d), it consists of an interconnected ligament network with ligament size l and solid fraction φ. Scanning electron microscope (SEM) images show a typical morphology with $l \approx 50$ nm and $\varphi \approx 0.3$ (b, c).

metals remain unexplored. This work bridges this gap by presenting single crystal microcompression simulations of NPG with crystal plasticity. In other words, although similar computational approaches exist for bulk metals, a systematic modeling framework tailored to nanoporous metals is still lacking. This work addresses that gap and further incorporates crystal plasticity to capture orientation effects, which remain largely unexplored in the context of NPG. To primarily aid experimental design, this computational study systematically examines the influence of four key extrinsic factors on plastic deformation across large strain regimes:

1. Pillar height-to-diameter ratio ($1.5 \leq h/d \leq 2.5$)
2. Taper angle ($0 \leq \theta \leq 4°$)
3. Friction coefficient ($0.0 \leq \mu \leq 0.2$)
4. Misalignment angle ($0 \leq \alpha \leq 2°$)

Fig. 1 schematically illustrates NPG at micro- and nanoscales. On the microscale, NPG is polycrystalline, while on the nanoscale, it features an interconnected ligament network characterized by ligament size l and solid fraction φ. For the computational plasticity study, the network is represented as a single crystal diamond-like lattice.

2. Materials and experimental methods

NPG, as used here, is typically produced via dealloying, where the less noble component of an alloy is selectively removed, leaving a bicontinuous gold network [5,65]. Ag-Au is the most common precursor, with silver dissolved in an acid or electrochemical bath. This process forms an interconnected network of nanoscale ligaments and pores, as shown in the scanning electron microscope (SEM) images in Fig. 1 (b, c), with morphology tunable through processing conditions. The solid fraction φ usually ranges from 0.2 to 0.4, while as-dealloyed ligament sizes l are 10-50 nm. Post-processing treatments like thermal annealing promote coarsening (50-500 nm), while electrochemical treatments allow precise ligament size control via applied potential or electrolyte composition.

The single crystal microcompression method involves fabricating micropillars with well-defined dimensions and crystal orientations, followed by uniaxial compression using a nanoindenter equipped with a flat punch. Focused ion beam (FIB) milling is employed to shape individual micropillars with controlled aspect ratios, typically ranging from 2:1 to 4:1 (height-to-diameter) [30–34,37,38]. While FIB milling ensures precise pillar fabrication, it often introduces a slight taper, preventing perfectly straight pillar geometries [52,54,55]. The taper angle θ is defined as

$$\theta = \tan^{-1}\left(\frac{d - d_0}{2h}\right), \tag{1}$$

where d is the pillar's constant top diameter, d_0 is the base diameter, and h is the pillar height. Additionally, a small curvature at the pillar base is commonly observed due to ion milling effects, which can influence stress distributions and deformation behavior [43,52,54,55]. With few exceptions [23,30], crystal orientations in NPG microcompression studies are often unspecified, as the material yielding is generally considered orientation-independent. Compression tests are conducted under controlled displacement rates, typically between 10^{-4} to 10^{-2} 1/s, ensuring quasi-static loading conditions. Stress-strain curves are constructed from recorded load and displacement, with engineering stress as force divided by the initial top cross-sectional area and engineering strain as displacement normalized by pillar height. Another key experimental challenge is ensuring proper alignment between the pillar top face and the flat punch. The misalignment angle θ, defined as the angle between the pillar top face and the indenter face, is given by

$$\alpha = \tan^{-1}\left(\frac{\Delta h}{d}\right), \tag{2}$$

where Δh is the height difference across the indenter due to tilt. For bulk metals, even minor misalignment of 1-2° can cause uneven stress distributions, leading to asymmetric deformation. To minimize this, careful sample calibration must be employed prior to testing.

3. Simulation methods

3.1. Constitutive model

The crystal plasticity finite element method (CPFEM), based on Huang's formulation [66], is used to describe the microcompression response, accounting for finite strain and rotation. To distinguish between elastic $\mathbf{F}_\mathrm{e}$ and plastic $\mathbf{F}_\mathrm{p}$ deformation components, the deformation gradient is multiplicatively decomposed as $\mathbf{F} = \mathbf{F}_\mathrm{e}\mathbf{F}_\mathrm{p}$. The material's stress state is then determined employing the generalized Hooke's law, expressed as $\mathbf{S} = \mathbb{C} : \mathbf{E}$. This formulation relates the elastic Green–Lagrange strain $\mathbf{E}$ to the second Piola–Kirchhoff stress $\mathbf{S}$ through the elastic stiffness tensor $\mathbb{C}$. Computed using the identity tensor $\mathbf{I}$, the Green–Lagrange strain is expressed as $\mathbf{E} = 1/2\left(\mathbf{F}_\mathrm{e}^\mathrm{T}\mathbf{F}_\mathrm{e} - \mathbf{I}\right)$. The elastic stiffness tensor $\mathbb{C}$ reflects the symmetry of the underlying crystal lattice, reducing the number of independent elastic constants to three (C_{11}, C_{12}, and C_{44}). Plastic deformation, governed by dislocation slip, is described by the plastic velocity gradient $\mathbf{L}_\mathrm{p}$. At this point, the actual crystal plasticity sets in through the accumulation of slip on multiple slip systems. The plastic velocity gradient is expressed as the sum of the slip rates $\dot{\gamma}^\alpha$ over all N_s slip systems

$$\mathbf{L}_\mathrm{p} = \dot{\mathbf{F}}_\mathrm{p}\mathbf{F}_\mathrm{p}^{-1} = \sum_{\alpha=1}^{N_\mathrm{s}} \dot{\gamma}^\alpha\, \mathbf{m}^\alpha \otimes \mathbf{n}^\alpha, \tag{3}$$

where $\mathbf{m}^\alpha$ represents the slip direction and $\mathbf{n}^\alpha$ denotes the slip plane normal for a given slip system α [67]. To qualify material hardening, a phenomenological description is deployed. On each slip system, the shear rate progresses according to the power law proposed by [68–70]

Table 1
Elastic constants and crystal plasticity parameters of NPG as considered in [30,66,71,72], assuming a solid fraction of $\varphi = 0.3$ and a ligament size of $l = 50$ nm. Plastic deformation occurs on the 12 octahedral fcc slip systems $\{111\}\langle 110\rangle$.

Property	Value	Unit
C_{11}	186	GPa
C_{12}	157	GPa
C_{44}	42	GPa
$\dot{\gamma}_0$	0.001	1/s
m	0.1	-
h_0	2000	MPa
τ_0	50	MPa
τ_s	199	MPa
q	1.0	-

$$\dot{\gamma}^{\alpha} = \dot{\gamma}_0 \left| \frac{\tau^{\alpha}}{g^{\alpha}} \right|^{\frac{1}{m}} \operatorname{sgn}(\tau^{\alpha}) \,, \tag{4}$$

where $\dot{\gamma}_0$ is the reference shear rate and τ^{α} the resolved shear stress opposed to the current strength g^{α} or critical resolved shear stress (CRSS). Strain rate sensitivity is characterized by the material parameter m. The influence of slip system β on the hardening behavior of system α is captured in the CRSS evolution by

$$\dot{g}^{\alpha} = \sum_{\beta=1}^{N_s} h_{\alpha\beta}\, \dot{\gamma}^{\beta} \,, \tag{5}$$

where $h_{\alpha\beta} = q\, h(\gamma)$ is the interaction hardening matrix with the functional form of

$$h(\gamma) = h_0 \operatorname{sech}^2 \left| \frac{h_0 \gamma}{\tau_s - \tau_0} \right| \,, \tag{6}$$

determining the micromechanical interaction between the different systems through the constant q. This constant sets the level of latent hardening as compared to self hardening. For all slip systems, the initial hardening modulus h_0, saturation strength τ_s, and initial strength τ_0 are identical.

For time integration, the CPFEM model is implemented in an implicit code (Abaqus/Standard) via a material subroutine [66]. Table 1 summarizes the elastic and crystal plasticity parameters for the face-centered cubic (fcc) NPG. The elastic constants C_{11}, C_{12}, and C_{44}, along with $\dot{\gamma}_0$ and h_0, follow [71,72]. A typical strain rate sensitivity of $m = 0.1$ is adopted, while a latent-to-self-hardening ratio of $q = 1$ indicates the absence of latent hardening [66]. The initial effective CRSS τ_0 and saturation strength τ_s are fitted to experimental stress-strain data from microcompression tests reported in [30], assuming a solid fraction of $\varphi = 0.3$ and a ligament size of $l = 50$ nm. It should be noted that, although ligament size and solid fraction are known to strongly affect the mechanical behavior of NPG, a parametric study of these intrinsic variables is beyond the scope of the present work due to computational cost. The chosen values represent typical experimental conditions and provide a meaningful basis for assessing deformation mechanisms focusing on extrinsic effects. A more comprehensive investigation into the collective interplay of ligament size, solid fraction, and crystal orientation is currently underway in a separate study. In contrast to molecular dynamics (MD) simulations, which are frequently used to investigate the mechanical behavior of NPG [13,15,21], the adopted CPFEM approach offers a more computationally efficient but still physically interpretable framework, well suited for systematically exploring orientation effects and deformation trends.

3.2. *Microstructure model and boundary conditions*

Fig. 2 illustrates the complete NPG micropillar models under compression, featuring a height-to-diameter ratio of $h/d = 2.0$ (a) and a taper angle of $\theta = 4°$ (c). The solid fraction is assigned to $\varphi = 0.3$. For comparison, traditional single crystal bulk gold samples are shown in Fig. 2 (b) and (d), alongside corresponding half-sections of all models in (e-h). The porous microstructure adopts a face-centered cubic (fcc) diamond-type lattice, which, despite simplifications, captures key geometric features relevant for mechanical response [57]. Additionally, the lattice provides ease of implementation and full parametric control over ligament geometry. It should be noted that preliminary simulations with both smaller and larger pillar diameters resulted in only minor variations in the stress-strain response, likely due to the regularity of the fcc-type microstructure. The chosen pillar diameter thus offers a good balance between model accuracy and computational efficiency. For experimental insights into this size effect in NPG micropillars, see [34]. To replicate the characteristic rounded morphology of NPG pores, ligament junctions incorporate curvature approximately equal to the ligament diameter. The pillars are modeled as cylindrical with a slight taper angle of up to 4° and rest on a larger substrate with a diameter twice that of the pillar. A subtle curvature at the pillar base, approximately 10% of the pillar diameter, is also incorporated. The substrate height-to-diameter ratio is approximately 1:4. Both the pillars and the substrate share the same crystallographic orientation and material parameters.

Compression is applied via a rigid surface positioned above the pillar, with a Coulomb friction coefficient of up to 0.2 between the two surfaces [43]. The misalignment angle between the punch and the pillar is restricted to $\leq 2°$. The NPG mesh approaches two million tetrahedral elements (C3D4) with linear shape functions and full integration, depending on the extrinsic shape effects analyzed. In contrast, the bulk mesh contains only a fraction of that, utilizing hexahedral elements (C3D8) with linear shape functions and full integration. Boundary conditions are set by fully constraining the substrate's bottom nodes, while the rigid surface moves downward in a displacement-controlled mode, mimicking typical experimental conditions. A strain rate of 10^{-3} 1/s is applied, and the pillars are compressed up to a total strain of $\varepsilon = 30\%$. Two initial crystal orientations are examined: the kinematically softer [001] ([010] $\parallel y$) and the kinematically harder $[\bar{1}11]$ ([110] $\parallel y$), both aligned with the compression z-direction. While the [001] orientation remains highly stable under compression, the $[\bar{1}11]$ orientation is more susceptible to crystallographic reorientation under the given boundary conditions [23,43].

4. Results and discussion

4.1. *Orientation-dependent aspect ratio and taper effect*

The predicted stress-strain curves in Fig. 3 (a) reveal the influence of aspect ratio and crystallographic orientation on the microcompression response, assuming frictionless contact. All pillars exhibit similar initial elasticity and yield around 40 MPa, but their post-yield behavior varies. The [001] orientation shows a moderate transition into plasticity, while the $[\bar{1}11]$ orientation exhibits pronounced strain hardening. Geometric effects further influence strain hardening and stability. Lower aspect ratio pillars ($h/d = 1.5$) exhibit higher strain hardening, especially in the $[\bar{1}11]$ orientation, enhancing resistance to strain localization. In contrast, taller pillars ($h/d = 2.5$) show gradual hardening followed by a stress drop at large strains, indicative of plastic buckling. This is most pronounced in the $[\bar{1}11]$ orientation, suggesting increased instability at higher aspect ratios. Fig. 4 (a) and (e) show corresponding von Mises stress contours for $h/d = 2.0$ at $\varepsilon = 20\%$, highlighting orientation-dependent differences. These findings suggest that for stable deformation in NPG micropillars, aspect ratios of $h/d \leq 2.0$ are preferable. While crystallographic orientation influences post-yield behavior, mechanical stability is mainly governed by geometric factors.

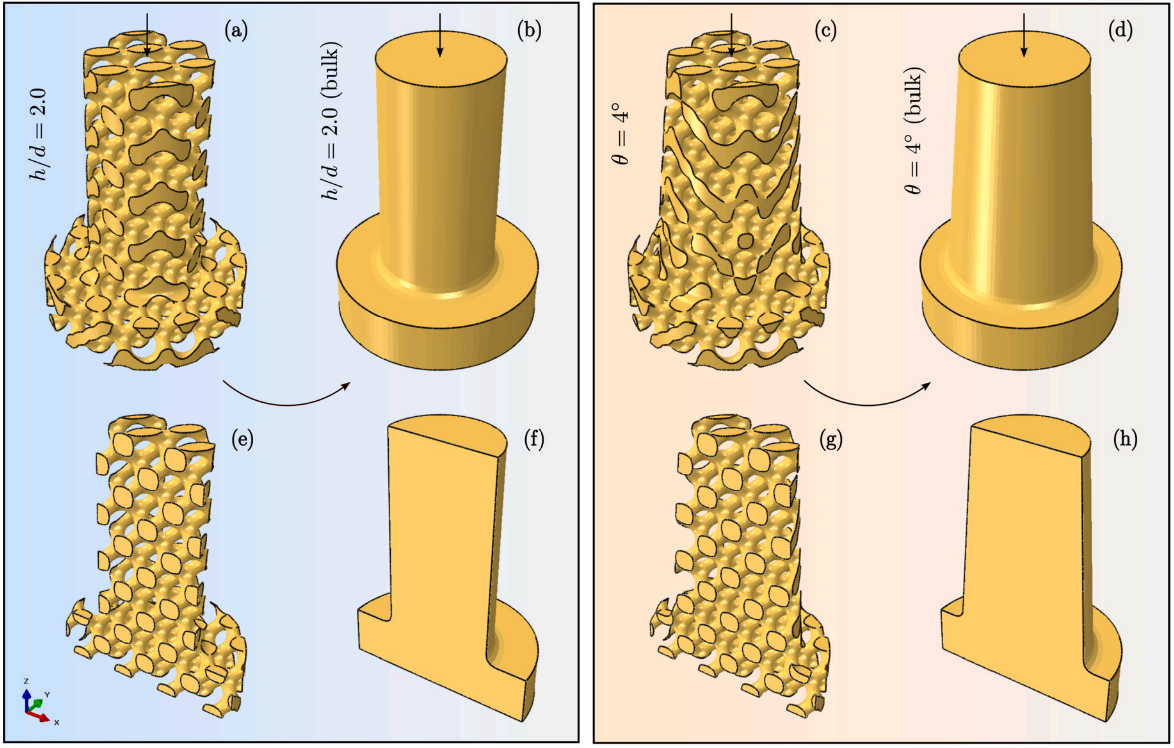

Fig. 2. Full microstructure models of NPG micropillars in compression tests with a height-to-diameter ratio of $h/d = 2.0$ (a) and a taper angle of $\theta = 4°$ (c), assuming a solid fraction of $\varphi = 0.3$. Single crystal bulk samples are depicted in (b) and (d). All pillars rest on a substrate with slight base curvature. The corresponding half-sections are presented in (e-h).

Fig. 3 (b) represents the predicted stress-strain response of bulk micropillars for comparison with their nanoporous counterparts. The bulk material exhibits significantly higher yield stress and strain hardening, with peak stresses exceeding 800 MPa. This is nearly an order of magnitude greater than nanoporous pillars, emphasizing the strength-reducing effect of porosity. Despite this disparity, similar trends emerge regarding aspect ratio and crystallographic orientation. Shorter pillars ($h/d = 1.5$) achieve higher peak stresses and exhibit stronger strain hardening, particularly in the $[\bar{1}11]$ orientation. Taller pillars ($h/d = 2.5$) show more gradual hardening but are prone to softening and instability at large strains, especially in the $[\bar{1}11]$ orientation, whereas the [001] orientation remains largely unaffected by pillar shape. Matching stress contour plots for $h/d = 2.0$ are shown in Fig. 4 (b) and (f). A direct comparison reveals that porosity fundamentally alters deformation behavior. Bulk micropillars exhibit a well-defined peak stress followed by strain softening or continued hardening, whereas nanoporous pillars display more gradual stress evolution due to complex mechanisms such as ligament bending, localized plasticity, and densification. The relative insensitivity of NPG to crystallographic orientation further underscores the dominance of its intricate architecture over lattice anisotropy. These findings suggest the need to consider both geometric and material factors when designing NPG-based microstructures for mechanical applications.

Fig. 3 (c) examines the effect of initial taper angle on the stress-strain response of NPG micropillars with an aspect ratio of $h/d = 2.0$. As the taper increases from $\theta = 0°$ to $\theta = 4°$, noticeable changes in elastic modulus, yield strength, and strain hardening occur, likely affected by a slight change in pillar volume since the top diameter remains fixed, see Eq. (1). Alternatively, the stress can be defined using the mean cross-sectional area $\bar{A} = (\pi \bar{d}^2)/4$, with the mean diameter $\bar{d} = (d + d_0)/2$, yielding a more consistent elastic modulus and plastic response by accounting for a true tapering effect. In both [001] and $[\bar{1}11]$ orientations, greater taper enhances stiffness, peak stress, and promotes a more gradual hardening response, suggesting improved stress distribution, see Fig. 4 (c) and (g). This effect may delay strain localization and improve deformation resistance, with the $[\bar{1}11]$ orientation showing slightly stronger strengthening effects, indicating an interplay between crystallography and geometric constraints. Based on SEM images of NPG after microcompression [17], strain localization has been observed, specifically in the form of dislocation slip bands and lines near ligament junctions. While the present work focuses on extrinsic effects during micropillar compression, a detailed analysis of stress and strain localization within the ligaments is part of a separate ongoing study. A moderate taper ($\theta \approx 2°$) appears beneficial, balancing stress localization mitigation with realistic deformation behavior. A slight taper prevents premature buckling and barreling while preserving the intrinsic mechanical properties of NPG. However, excessive taper should be avoided, as it may introduce non-uniform stress distributions, deviating from the idealized response of straight-sided micropillars.

For bulk micropillars, the taper angle significantly affects the microcompression response, as shown in Fig. 3 (d). Similar to NPG, increasing the taper angle enhances elastic modulus, peak stress, and strain hardening. However, these effects are more pronounced in bulk micropillars due to their higher inherent strength. In NPG, deformation is dominated by ligament-scale plasticity and strain localization, which mitigates taper-induced strengthening. Additionally, porosity limits strain hardening, as deformation is driven more by ligament bending and compaction than by pure plastic deformation. A key difference is the pronounced buckling in untapered bulk micropillars, particularly in the $[\bar{1}11]$ orientation, where a sharp stress drop indicates global instability rather than uniform plastic flow. In contrast, NPG micropillars exhibit more gradual softening due to ligament-scale plasticity, reducing susceptibility to catastrophic buckling. The absence of taper allows imperfections to trigger bending and stress non-uniformities, leading to premature failure. Softer orientations like [001] show more stable deformation due to uniform slip system activation, see Fig. 4 (d) and (h). Introducing a slight taper ($\theta \approx 2 - 4°$) stabilizes stress distributions, delays buckling, and promotes controlled plastic flow. The increased base cross-section enhances resistance to bending, allowing harder orientations to sustain

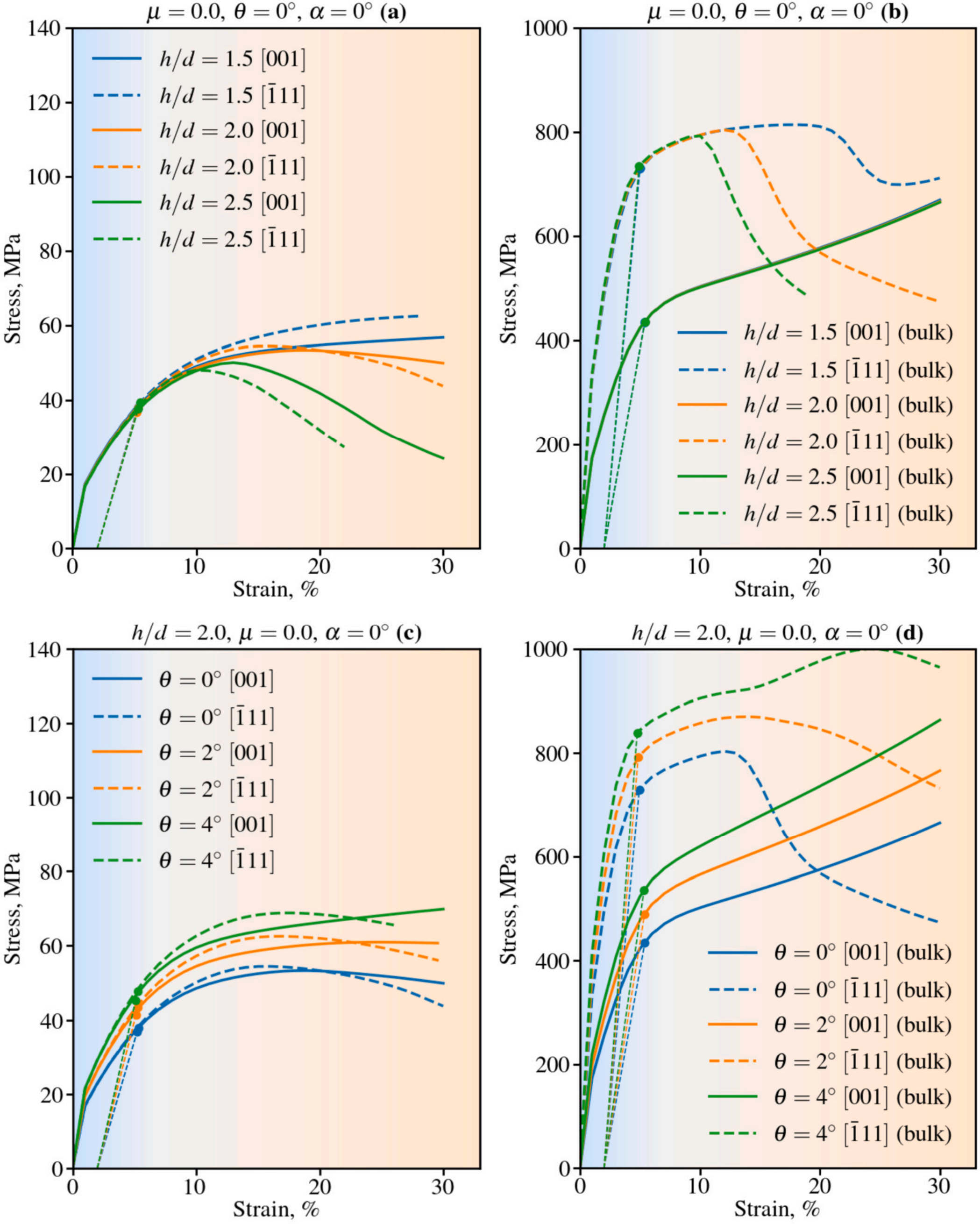

Fig. 3. Predicted stress-strain curves for varying pillar height-to-diameter ratios h/d in (a) and (b), and different taper angles θ in (c) and (d). The single crystal bulk responses are depicted in (b) and (d). All predictions assume a solid fraction of $\varphi = 0.3$ (NPG), a ligament size of $l = 50$ nm, and initial crystal orientations of [001] and [$\bar{1}11$]. The yield point is identified at a 2% strain offset.

higher stresses before softening. While tapering improves mechanical stability in NPG micropillars, its impact is again secondary to the dominant role of ligament network mechanics. Unlike bulk samples, NPG pillars experience localized plasticity rather than global buckling, resulting in distributed strain hardening that prevents sudden stress drops.

4.2. *Orientation-dependent friction and misalignment effect*

Friction at the NPG micropillar-indenter interface significantly alters the stress-strain response. As seen in Fig. 5 (a), increasing μ from 0.0 to 0.2 raises the flow stress, especially at higher strains, due to friction-induced constraints. This restriction limits lateral expansion, alters the stress state, and delays plastic deformation, with the effect being more pronounced in the [$\bar{1}11$] orientation due to its higher CRSS. Compared to tapering, friction plays a distinct yet complementary role. While tapering stabilizes micropillars and prevents buckling, friction enhances apparent strength by increasing confinement. However, excessive friction may create stress gradients, leading to non-uniform deformation or shear localization near the contact region. To ensure a uniform stress state in experiments, controlling friction conditions is crucial. Using lubricated indenters or minimizing misalignment can help, with a recommended minimal friction coefficient of $\mu = 0.05$ to balance confinement effects while avoiding excessive stress gradients. Pairing moderate taper with controlled friction can further improve the reliability and reproducibility of mechanical responses.

Friction also significantly influences the deformation behavior of bulk micropillars, as indicated in Fig. 5 (b). Increasing μ from 0.0 to 0.2 raises peak stress and stabilizes the stress-strain response, particularly

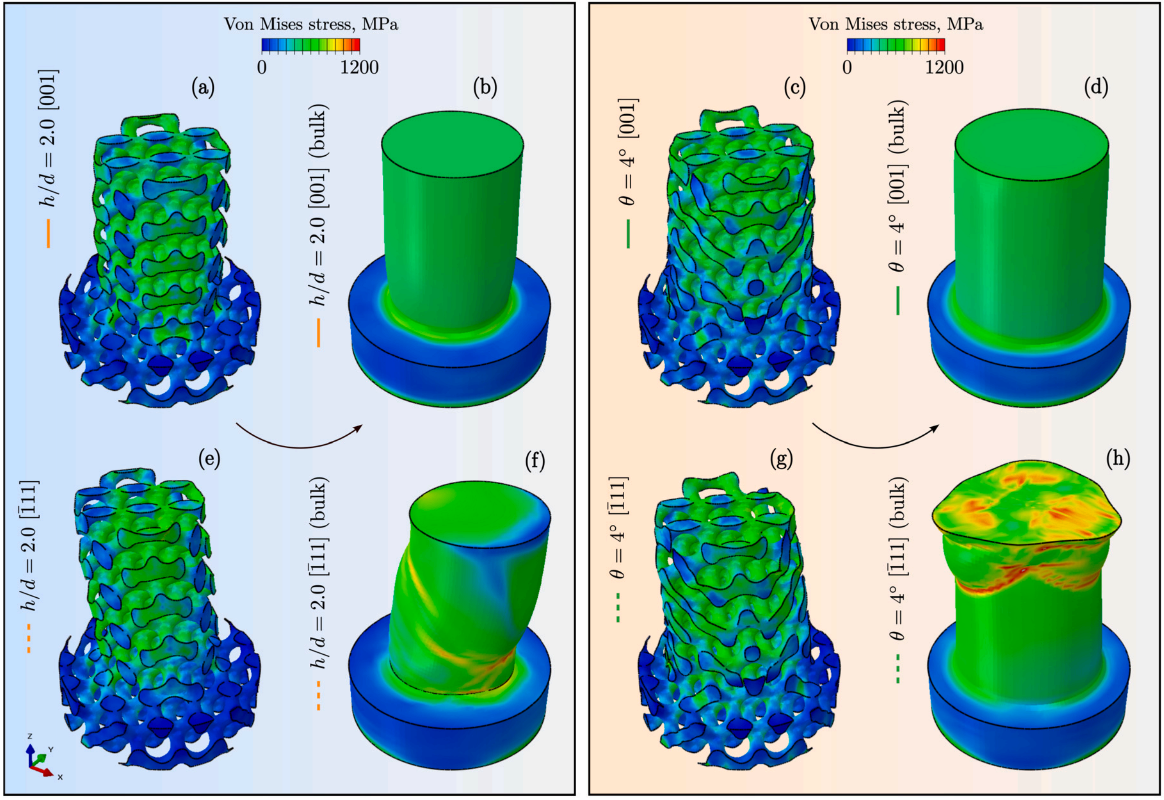

Fig. 4. Predicted von Mises stress contour plots with a pillar height-to-diameter ratio of $h/d = 2.0$ (a, b) and a taper angle of $\theta = 4°$ (c, d) at a compression strain of $\varepsilon = 20\%$. The single crystal bulk responses are depicted in (b) and (d). Initial crystal orientations are classified as weak for [001] (a-d) and strong for [$\bar{1}$11] (e-h). All predictions assume a solid fraction of $\varphi = 0.3$ (NPG) and a ligament size of $l = 50$ nm.

in the [$\bar{1}$11] orientation, where severe buckling at $\mu = 0.0$ is largely mitigated. Interestingly, at higher friction levels ($\mu = 0.2$) and larger deformation, the stress-strain curves become nearly independent of orientation, suggesting friction suppresses orientation-dependent instabilities. While a similar trend is observed in NPG micropillars, the friction effect is less pronounced due to the dominant role of ligament-scale plasticity. This contrast further highlights how intrinsic microstructure governs mechanical stability. Bulk pillars are prone to buckling, whereas NPG micropillars maintain stable deformation even at low friction. In summary, while both bulk and NPG micropillars exhibit friction-dependent behavior, their underlying deformation mechanisms differ. Understanding these differences could aid in designing micropillar experiments that more accurately reflect material behavior under compression.

Fig. 5 (c) presents the impact of misalignment on NPG micropillars under frictionless conditions. Unlike taper, which affects buckling stability, misalignment shifts the loading axis, altering stress distribution and deformation mechanisms. Increasing α from 0 to 2° slightly reduces peak stress and strain hardening, promoting asymmetric deformation. The apparent elastic modulus also decreases with misalignment, indicating increased bending and off-axis deformation. Compared to friction, misalignment has a weaker influence on strengthening, emphasizing the dominant role of boundary conditions. To minimize measurement artifacts, a small misalignment angle (e.g., $\alpha \leq 1°$) is recommended for accurate experiments.

Fig. 5 (d) illustrates the impact of misalignment on the stress-strain response of bulk micropillars. Increasing α reduces the elastic modulus, as seen in the decreasing initial slope of the curves, consistent with NPG micropillars. This suggests that misalignment introduces compliance effects, as the indenter must first establish full contact, and the progressively increasing contact area reduces the apparent stiffness. The [$\bar{1}$11] orientation exhibits pronounced buckling across all misalignment angles, while the softer [001] orientation transitions more gradually into plastic flow, with lower α promoting a more uniform stress distribution. Compared to friction effects, which slightly increase modulus and delay buckling, misalignment has the opposite effect, reducing stiffness and accelerating instability. This emphasizes the intricate interplay between experimental alignment, friction, and crystal anisotropy in micropillar compression tests.

5. Conclusions

In summary, a computational plasticity approach is employed to systematically explore four key extrinsic effects, including pillar height-to-diameter ratio ($1.5 \leq h/d \leq 2.5$), taper angle ($0 \leq \theta \leq 4°$), friction coefficient ($0.0 \leq \mu \leq 0.2$), and misalignment angle ($0 \leq \alpha \leq 2°$), on the single crystal NPG microcompression response, extending well beyond yielding. Key findings include:

- NPG behaves similarly to its bulk counterpart under the extrinsic effects but is significantly less prone to post-yield buckling for harder, more unstable orientations.
- To maintain stability, a pillar height-to-diameter ratio of $1.5 \leq h/d \leq 2$ is recommended as well as a taper angle of $\theta \approx 2°$ to prevent extensive stiffening and yielding.
- Even minimal friction ($\mu \leq 0.05$) enhances structural stability during compression testing.
- Misalignment primarily dictates buckling, necessitating a small α, e.g. $\alpha \leq 1°$, to also mitigate underestimation of the elastic modulus.

CRediT authorship contribution statement

Tim Fischer: Writing – original draft, Visualization, Validation, Software, Methodology, Investigation, Formal analysis, Conceptualization. **Norbert Huber:** Writing – review & editing, Supervision, Resources, Project administration, Funding acquisition.

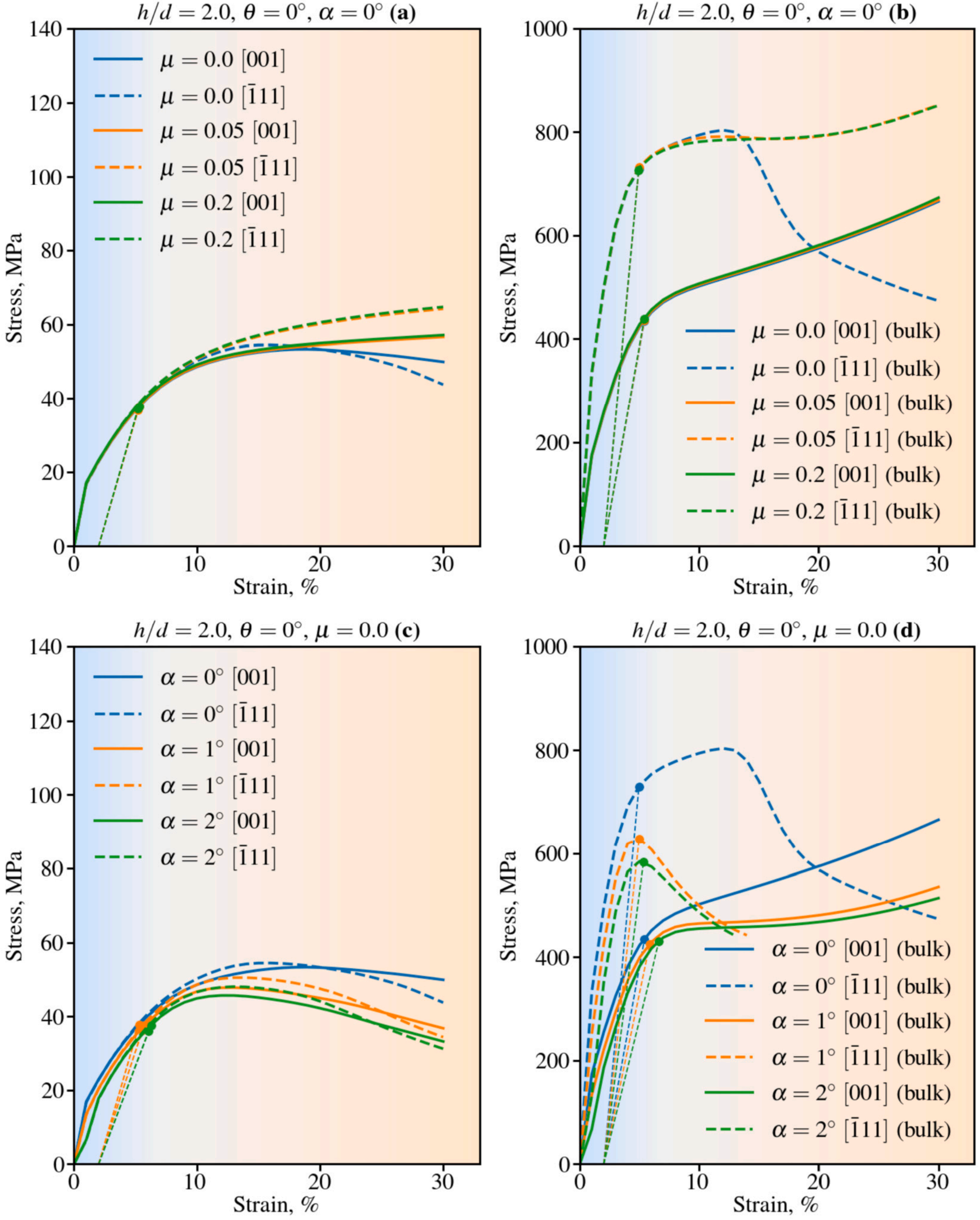

Fig. 5. Predicted stress-strain curves for varying friction coefficients μ in (a) and (b), and misalignment angles α in (c) and (d). The single crystal bulk responses are depicted in (b) and (d). All predictions assume a solid fraction of $\varphi = 0.3$ (NPG), a ligament size of $l = 50$ nm, and initial crystal orientations of [001] and [$\bar{1}$11]. The yield point is identified at a 2% strain offset.

Declaration of competing interest

The authors declare that they have no known competing financial interests or personal relationships that could have appeared to influence the work reported in this paper.

Acknowledgements

This work was supported by the Deutsche Forschungsgemeinschaft (DFG, German Research Foundation) through the Cluster of Excellence EXC3120 BlueMat: Water-Driven Materials and the Hamburg Centre for Integrated Multiscale Materials Systems (CIMMS). The authors gratefully acknowledge S. Shi (Hamburg University of Technology) for insightful discussions and the TUHH Computing Center for providing access to the high-performance computing (HPC) cluster. Special thanks are extended to C.F.O. Dahlberg (KTH Royal Institute of Technology, Sweden) for providing the material subroutine used in Abaqus, and to Y. Zhang (Hamburg University of Technology) for the SEM images. Publishing fees supported by the Funding Programme Open Access Publishing of Hamburg University of Technology (TUHH).

Data availability

Data will be made available on request.

References

[1] H.-J. Jin, J. Weissmüller, A material with electrically tunable strength and flow stress, Science 332 (6034) (2011) 1179–1182, https://doi.org/10.1126/science.1202190.

[2] H.-J. Jin, J. Weissmüller, Bulk nanoporous metal for actuation, Adv. Eng. Mater. 12 (8) (2010) 714–723, https://doi.org/10.1002/adem.200900329.

[3] J. Weissmüller, R.N. Viswanath, D. Kramer, P. Zimmer, R. Würschum, H. Gleiter, Charge-induced reversible strain in a metal, Science 300 (5617) (2003) 312–315, https://doi.org/10.1126/science.1081024.

[4] J. Biener, A. Wittstock, L. Zepeda-Ruiz, M. Biener, V. Zielasek, D. Kramer, R. Viswanath, J. Weissmüller, M. Bäumer, A. Hamza, Surface-chemistry-driven actuation in nanoporous gold, Nat. Mater. 8 (2009) 47–51, https://doi.org/10.1038/nmat2335.

[5] J. Weissmüller, R.C. Newman, H.-J. Jin, A.M. Hodge, J.W. Kysar, Nanoporous metals by alloy corrosion: formation and mechanical properties, Mater. Res. Soc. Bull. 34 (8) (2009) 577–586, https://doi.org/10.1557/mrs2009.157.

[6] H. Gleiter, J. Weissmüller, O. Wollersheim, R. Würschum, Nanocrystalline materials: a way to solids with tunable electronic structures and properties?, Acta Mater. 49 (4) (2001) 737–745, https://doi.org/10.1016/S1359-6454(00)00221-4.

[7] G. Wittstock, M. Bäumer, W. Dononelli, T. Klüner, L. Lührs, C. Mahr, L.V. Moskaleva, M. Oezaslan, T. Risse, A. Rosenauer, A. Staubitz, J. Weissmüller, A. Wittstock, Nanoporous gold: from structure evolution to functional properties in catalysis and electrochemistry, Chem. Rev. 123 (10) (2023) 6716–6792, https://doi.org/10.1021/acs.chemrev.2c00751.

[8] L.-Z. Liu, Y.-Y. Zhang, H. Xie, H.-J. Jin, Transition from homogeneous to localized deformation in nanoporous gold, Phys. Rev. Lett. 127 (2021) 095501, https://doi.org/10.1103/PhysRevLett.127.095501.

[9] L.-Z. Liu, Y.-Y. Zhang, H.-J. Jin, On correlation between the hardness-to-strength ratio and the plastic Poisson's ratio of nanoporous gold, Mater. Res. Lett. 11 (6) (2023) 454–461, https://doi.org/10.1080/21663831.2023.2181717.

[10] P. Wu, X.-L. Ye, L.-Z. Liu, H.-J. Jin, Monolayer oxide enhanced flow stress in nanoporous gold: the size dependence, Mater. Res. Lett. 6 (9) (2018) 508–514, https://doi.org/10.1080/21663831.2018.1486337.

[11] J.R. Greer, J.T. De Hosson, Plasticity in small-sized metallic systems: intrinsic versus extrinsic size effect, Prog. Mater. Sci. 56 (6) (2011) 654–724, https://doi.org/10.1016/j.pmatsci.2011.01.005.

[12] L.-Z. Liu, X.-L. Ye, H.-J. Jin, Interpreting anomalous low-strength and low-stiffness of nanoporous gold: quantification of network connectivity, Acta Mater. 118 (2016) 77–87, https://doi.org/10.1016/j.actamat.2016.07.033.

[13] S. Shi, Y. Li, B.-N. Ngo-Dinh, J. Markmann, J. Weissmüller, Scaling behavior of stiffness and strength of hierarchical network nanomaterials, Science 371 (6533) (2021) 1026–1033, https://doi.org/10.1126/science.abd9391.

[14] H.-J. Jin, L. Kurmanaeva, J. Schmauch, H. Rösner, Y. Ivanisenko, J. Weissmüller, Deforming nanoporous metal: role of lattice coherency, Acta Mater. 57 (9) (2009) 2665–2672, https://doi.org/10.1016/j.actamat.2009.02.017.

[15] X.-Y. Sun, G.-K. Xu, X. Li, X.-Q. Feng, H. Gao, Mechanical properties and scaling laws of nanoporous gold, J. Appl. Phys. 113 (2) (2013) 023505, https://doi.org/10.1063/1.4774246.

[16] N. Mameka, K. Wang, J. Markmann, E.T. Lilleodden, J. Weissmüller, Nanoporous gold—testing macro-scale samples to probe small-scale mechanical behavior, Mater. Res. Lett. 4 (1) (2016) 27–36, https://doi.org/10.1080/21663831.2015.1094679.

[17] H. Jeon, J. Markmann, S. Shi, Effects of structural hierarchy and size on mechanical behavior of nanoporous gold, Acta Mater. 273 (2024) 119954, https://doi.org/10.1016/j.actamat.2024.119954.

[18] H. Jeon, J.-H. Woo, E. Song, J.-Y. Kim, Ligament size effect in creep of nanoporous gold, Int. J. Plast. 150 (2022) 103192, https://doi.org/10.1016/j.ijplas.2021.103192.

[19] N.-R. Kang, E.-J. Gwak, H. Jeon, E. Song, J.-Y. Kim, Microstructural effect on time-dependent plasticity of nanoporous gold, Int. J. Plast. 109 (2018) 108–120, https://doi.org/10.1016/j.ijplas.2018.05.011.

[20] J. Sanchez, L. Dammann, L. Gallardo, Z. Li, M. Fröba, R.H. Meißner, H.A. Stone, P. Huber, Deformation dynamics of nanopores upon water imbibition, Proc. Natl. Acad. Sci. USA 121 (38) (2024) e2318386121, https://doi.org/10.1073/pnas.2318386121.

[21] B.-N.D. Ngô, A. Stukowski, N. Mameka, J. Markmann, K. Albe, J. Weissmüller, Anomalous compliance and early yielding of nanoporous gold, Acta Mater. 93 (2015) 144–155, https://doi.org/10.1016/j.actamat.2015.04.021.

[22] J. Weissmüller, H.-L. Duan, D. Farkas, Deformation of solids with nanoscale pores by the action of capillary forces, Acta Mater. 58 (1) (2010) 1–13, https://doi.org/10.1016/j.actamat.2009.08.008.

[23] D. Ma, P. Eisenlohr, E. Epler, C.A. Volkert, P. Shanthraj, M. Diehl, F. Roters, D. Raabe, Crystal plasticity study of monocrystalline stochastic honeycombs under in-plane compression, Acta Mater. 103 (2016) 796–808, https://doi.org/10.1016/j.actamat.2015.11.016.

[24] D. Ma, P. Eisenlohr, P. Shanthraj, M. Diehl, F. Roters, D. Raabe, Analytical bounds of in-plane Young's modulus and full-field simulations of two-dimensional monocrystalline stochastic honeycomb structures, Comput. Mater. Sci. 109 (2015) 323–329, https://doi.org/10.1016/j.commatsci.2015.07.041.

[25] J. Biener, A.M. Hodge, A.V. Hamza, Microscopic failure behavior of nanoporous gold, Appl. Phys. Lett. 87 (12) (2005) 121908, https://doi.org/10.1063/1.2051791.

[26] C.A. Volkert, E.T. Lilleodden, Size effects in the deformation of sub-micron au columns, Philos. Mag. 86 (33–35) (2006) 5567–5579, https://doi.org/10.1080/14786430600567739.

[27] J.R. Greer, W.C. Oliver, W.D. Nix, Size dependence of mechanical properties of gold at the micron scale in the absence of strain gradients, Acta Mater. 53 (6) (2005) 1821–1830, https://doi.org/10.1016/j.actamat.2004.12.031.

[28] R. Dou, B. Derby, The strength of gold nanowire forests, Scr. Mater. 59 (2) (2008) 151–154, https://doi.org/10.1016/j.scriptamat.2008.02.046.

[29] B. Wu, A. Heidelberg, J.J. Boland, Mechanical properties of ultrahigh-strength gold nanowires, Nat. Mater. 4 (7) (2005) 525–529, https://doi.org/10.1038/nmat1403.

[30] H. Jeon, S. Lee, J.-Y. Kim, Tension-compression asymmetry in plasticity of nanoporous gold, Acta Mater. 199 (2020) 340–351, https://doi.org/10.1016/j.actamat.2020.08.054.

[31] C.A. Volkert, E.T. Lilleodden, D. Kramer, J. Weissmüller, Approaching the theoretical strength in nanoporous au, Appl. Phys. Lett. 89 (6) (2006) 061920, https://doi.org/10.1063/1.2240109.

[32] Y.-Y. Zhang, L. Zou, L.-Z. Liu, H. Xie, C.-H. Li, H.-J. Jin, Mechanical properties of unidirectional nanoporous gold under compression, Acta Mater. 235 (2022) 118078, https://doi.org/10.1016/j.actamat.2022.118078.

[33] E.-J. Gwak, H. Jeon, E. Song, N.-R. Kang, J.-Y. Kim, Twinned nanoporous gold with enhanced tensile strength, Acta Mater. 155 (2018) 253–261, https://doi.org/10.1016/j.actamat.2018.06.009.

[34] Y. Wu, J. Markmann, E.T. Lilleodden, On the consequences of intrinsic and extrinsic size effects on the mechanical response of nanoporous au, Mater. Des. 232 (2023) 112175, https://doi.org/10.1016/j.matdes.2023.112175.

[35] D. Lee, X. Wei, X. Chen, M. Zhao, S. Jun, J. Hone, E.G. Herbert, W.C. Oliver, J.W. Kysar, Microfabrication and mechanical properties of nanoporous gold at the nanoscale, Scr. Mater. 56 (5) (2007) 437–440, https://doi.org/10.1016/j.scriptamat.2006.08.069.

[36] S. Van Petegem, S. Brandstetter, R. Maass, A.M. Hodge, B.S. El-Dasher, J. Biener, B. Schmitt, C. Borca, H. Van Swygenhoven, On the microstructure of nanoporous gold: an x-ray diffraction study, Nano Lett. 9 (3) (2009) 1158–1163, https://doi.org/10.1021/nl803799q.

[37] H. Guan, H. Xie, Z.-P. Luo, W.-K. Bao, Z.-S. You, Z. Jin, H.-J. Jin, Ultrastrong spinodoid alloys enabled by electrochemical dealloying and refilling, Proc. Natl. Acad. Sci. USA 120 (1) (2023) e2214773120, https://doi.org/10.1073/pnas.2214773120.

[38] J. Biener, A.M. Hodge, J.R. Hayes, C.A. Volkert, L.A. Zepeda-Ruiz, A.V. Hamza, F.F. Abraham, Size effects on the mechanical behavior of nanoporous au, Nano Lett. 6 (10) (2006) 2379–2382, https://doi.org/10.1021/nl061978i.

[39] Y. Wu, J. Markmann, E.T. Lilleodden, Electro-chemo-mechanical coupling of nanoporous gold at the microscale, Appl. Phys. Lett. 115 (25) (2019) 251602, https://doi.org/10.1063/1.5128049.

[40] J. Biener, A.M. Hodge, A.V. Hamza, L.M. Hsiung, J.H. Satcher, Nanoporous au: a high yield strength material, J. Appl. Phys. 97 (2) (2004) 024301, https://doi.org/10.1063/1.1832742.

[41] M. Benedetti, A. du Plessis, R. Ritchie, M. Dallago, N. Razavi, F. Berto, Architected cellular materials: a review on their mechanical properties towards fatigue-tolerant design and fabrication, Mater. Sci. Eng. R 144 (2021) 100606, https://doi.org/10.1016/j.mser.2021.100606.

[42] R. Xia, C. Xu, W. Wu, X. Li, X.-Q. Feng, Y. Ding, Microtensile tests of mechanical properties of nanoporous au thin films, J. Mater. Sci. 44 (17) (2009) 4728–4733, https://doi.org/10.1007/s10853-009-3731-1.

[43] D. Raabe, D. Ma, F. Roters, Effects of initial orientation, sample geometry and friction on anisotropy and crystallographic orientation changes in single crystal microcompression deformation: a crystal plasticity finite element study, Acta Mater. 55 (13) (2007) 4567–4583, https://doi.org/10.1016/j.actamat.2007.04.023.

[44] T. Loaiza, T. Fischer, R.P. Babu, P. Hedström, Micromechanical response of dual-hardening martensitic bearing steel before and after rolling contact fatigue, J. Mater. Res. Technol. 29 (2024) 4728–4734, https://doi.org/10.1016/j.jmrt.2024.02.142.

[45] S. Breumier, S. Sao-Joao, A. Villani, M. Lévesque, G. Kermouche, High strain rate micro-compression for crystal plasticity constitutive law parameters identification, Mater. Des. 193 (2020) 108789, https://doi.org/10.1016/j.matdes.2020.108789.

[46] S. Yan, H. Zhou, B. Xing, S. Zhang, L. Li, Q.H. Qin, Crystal plasticity in fusion zone of a hybrid laser welded al alloys joint: from nanoscale to macroscale, Mater. Des. 160 (2018) 313–324, https://doi.org/10.1016/j.matdes.2018.09.031.

[47] L. Chen, T.E. James Edwards, F. Di Gioacchino, W.J. Clegg, F.P. Dunne, M.-S. Pham, Crystal plasticity analysis of deformation anisotropy of lamellar tial alloy: 3d microstructure-based modelling and in-situ micro-compression, Int. J. Plast. 119 (2019) 344–360, https://doi.org/10.1016/j.ijplas.2019.04.012.

[48] S. Ha, S.H. Kayani, K. Lee, S. Park, J.G. Kim, J.B. Seol, H. Sung, Experimental and crystal plasticity finite element study of the deformation behavior of high-mn steel micropillars, Steel Res. Int. 94 (2) (2023) 2200254, https://doi.org/10.1002/srin.202200254.

[49] J. Wang, C. Yang, P.D. Hodgson, Strain gradients in cu–fe thin films and multilayers during micropillar compression, Mater. Sci. Eng. A 651 (2016) 146–154, https://doi.org/10.1016/j.msea.2015.10.105.

[50] D. Kupka, N. Huber, E. Lilleodden, A combined experimental-numerical approach for elasto-plastic fracture of individual grain boundaries, J. Mech. Phys. Solids 64 (2014) 455–467, https://doi.org/10.1016/j.jmps.2013.12.004.

[51] D. Li, R. Li, K. Yuan, A. Chen, N. Guo, C. Xu, W. Zhang, In-plane combination of micropillars with distinct aspect ratios to resist overload-induced adhesion failure, Adv. Sci. 11 (28) (2024) 2400972, https://doi.org/10.1002/advs.202400972.

[52] A. Cornec, E. Lilleodden, Numerical analysis of micropillar compression behaviour and stress-strain curve estimation verified on glass fused silica, Mater. Today Commun. 33 (2022) 104971, https://doi.org/10.1016/j.mtcomm.2022.104971.

[53] S. Bargmann, C. Soyarslan, E. Husser, N. Konchakova, Materials based design of structures: computational modeling of the mechanical behavior of gold-polymer nanocomposites, Mech. Mater. 94 (2016) 53–65, https://doi.org/10.1016/j.mechmat.2015.11.008.

[54] A. Cornec, E. Lilleodden, Stress-strain curve estimation from micropillar compression with transverse contraction effect, Mater. Today Commun. 41 (2024) 110396, https://doi.org/10.1016/j.mtcomm.2024.110396.

[55] H. Zhang, B. Schuster, Q. Wei, K. Ramesh, The design of accurate micro-compression experiments, Scr. Mater. 54 (2) (2006) 181–186, https://doi.org/10.1016/j.scriptamat.2005.06.043.

[56] B. Roschning, N. Huber, Scaling laws of nanoporous gold under uniaxial compression: effects of structural disorder on the solid fraction, elastic Poisson's ratio, young's modulus and yield strength, J. Mech. Phys. Solids 92 (2016) 55–71, https://doi.org/10.1016/j.jmps.2016.02.018.

[57] N. Huber, R. Viswanath, N. Mameka, J. Markmann, J. Weißmüller, Scaling laws of nanoporous metals under uniaxial compression, Acta Mater. 67 (2014) 252–265, https://doi.org/10.1016/j.actamat.2013.12.003.

[58] J. Li, C. Tian, B. Lu, Y. Xian, R. Wu, G. Hu, R. Xia, Deformation behavior of nanoporous gold based composite in compression: a finite element analysis, Compos. Struct. 211 (2019) 229–235, https://doi.org/10.1016/j.compstruct.2018.12.046.

[59] E. Griffiths, J. Wilmers, S. Bargmann, B.D. Reddy, Nanoporous metal based composites: giving polymers strength and making metals move, J. Mech. Phys. Solids 137 (2020) 103848, https://doi.org/10.1016/j.jmps.2019.103848.

[60] K. Hua, M. Ziehmer, K. Wang, E.T. Lilleodden, Nanoporous gold: 3d structural analyses of representative volumes and their implications on scaling relations of mechanical behaviour, Philos. Mag. 96 (32–34) (2016) 3322–3335, https://doi.org/10.1080/14786435.2016.1222087.

[61] L. Lührs, B. Zandersons, N. Huber, J. Weissmüller, Plastic Poisson's ratio of nanoporous metals: a macroscopic signature of tension–compression asymmetry at the nanoscale, Nano Lett. 17 (10) (2017) 6258–6266, https://doi.org/10.1021/acs.nanolett.7b02950.

[62] J. Jiao, N. Huber, Deformation mechanisms in nanoporous metals: effect of ligament shape and disorder, Comput. Mater. Sci. 127 (2017) 194–203, https://doi.org/10.1016/j.commatsci.2016.10.035.

[63] C. Soyarslan, S. Bargmann, M. Pradas, J. Weissmüller, 3d stochastic bicontinuous microstructures: generation, topology and elasticity, Acta Mater. 149 (2018) 326–340, https://doi.org/10.1016/j.actamat.2018.01.005.

[64] H.-H. Cho, Y.-C.K. Chen-Wiegart, D.C. Dunand, Finite element analysis of mechanical stability of coarsened nanoporous gold, Scr. Mater. 115 (2016) 96–99, https://doi.org/10.1016/j.scriptamat.2016.01.011.

[65] J. Erlebacher, M.J. Aziz, A. Karma, N. Dimitrov, K. Sieradzki, Evolution of nanoporosity in dealloying, Nature 410 (6827) (2001) 450–453, https://doi.org/10.1038/35068529.

[66] Y. Huang, A user-material subroutine incorporating single crystal plasticity in the abaqus finite element program, Harvard University Report Mech. 178, 1991.

[67] E. Schmid, W. Boas, Kristallplastizität – Mit besonderer Berücksichtigung der Metalle, vol. 17, Springer-Verlag, Berlin Heidelberg, 1935.

[68] J. Hutchinson, Bounds and self-consistent estimates for creep of polycrystalline materials, Proc. Royal Soc. A, Math. Phys. Eng. Sci. 348 (1652) (1976) 101–127.

[69] D. Peirce, R. Asaro, A. Needleman, Material rate dependence and localized deformation in crystalline solids, Acta Metall. 31 (12) (1983) 1951–1976, https://doi.org/10.1016/0001-6160(83)90014-7.

[70] S.R. Kalidindi, Incorporation of deformation twinning in crystal plasticity models, J. Mech. Phys. Solids 46 (2) (1998) 267–290, https://doi.org/10.1016/S0022-5096(97)00051-3.

[71] J.P. Hirth, J. Lothe, Theory of Dislocations, 2nd edition, Wiley, New York, 1982.

[72] D. Lee, X. Wei, M. Zhao, X. Chen, S.C. Jun, J. Hone, J.W. Kysar, Plastic deformation in nanoscale gold single crystals and open-celled nanoporous gold, Model. Simul. Mater. Sci. Eng. 15 (1) (2006) S181, https://doi.org/10.1088/0965-0393/15/1/S15.